Journal of Alloys and Compounds 899 (2022) 163278

Contents lists available at ScienceDirect

Journal of Alloys and Compounds

journal homepage: www.elsevier.com/locate/jalcom

Crystal structure and thermochromic behavior of the quasi-0D lead-free organic-inorganic hybrid compounds $(C_7H_9NF)_8M_4I_{16}$ (M = Bi, Sb)

X.C. Zhao[a], Y.K. Fu[a], Y.L. Lei[b], Winnie Wong-Ng[c], C. Wang[a], Q. Gu[a], W. Zhou[a], S.Y. Wang[b,*], W.F. Liu[a,*]

[a] Tianjin Key Laboratory of Low Dimensional Materials Physics and Preparing Technology, School of Science, Tianjin University, Tianjin 300072, China
[b] College of Physics and Material Science, Tianjin Normal University, Tianjin 300074, China
[c] Materials Measurement Science Division, National Institute of Standards and Technology, Gaithersburg, MD 20899, USA

ARTICLE INFO

Article history:
Received 20 October 2021
Received in revised form 10 December 2021
Accepted 13 December 2021
Available online 21 December 2021

Keywords:
Thermochromic
Hybrid inorganic organic $(C_7H_9NF)_8M_4I_{16}$ (M = Bi, Sb)
Crystal structure
Bandgap
Lead-free

ABSTRACT

The quasi 0D lead-free thermochromic organic-inorganic hybrid single crystals $(C_7H_9NF)_8M_4I_{16}$ (M = Bi, Sb) were synthesized by a conventional solvothermal reaction method. The crystal structures were analyzed using single crystal X-ray diffraction (SXRD). Interestingly, as the temperature increases, the $(C_7H_9NF)_8M_4I_{16}$ (M = Bi, Sb) crystals exhibit a peculiar thermochromic phenomenon. In order to explore the phenomenon of thermochromism, temperature dependent ultraviolet–visible-near-infrared (UV–vis–NIR) absorption spectra were measured. The bandgaps of $(C_7H_9NF)_8Sb_4I_{16}$ and $(C_7H_9NF)_8Bi_4I_{16}$ at room temperature are 2.34 eV and 2.1 eV, respectively, and they gradually decrease as the temperature increases. Combined with ab initio molecular dynamics (AIMD), the reduction of the bandgap at higher temperature and the occurrence of thermochromism could be caused by the stronger electronic activity (thermal excitation). The thermochromic characteristics of these low-dimensional organic-inorganic hybrid metal halides will provide alternative materials for smart windows temperature sensors, visual thermometers, and daylight control glasses and beyond.

1. Introduction

Thermochromism, which has been studied for centuries, denotes the rare phenomenon of a color change that is dependent on the temperature variation. Due to the potential applications of thermochromism in smart windows, temperature sensors, visual thermometers and daylight control glass, global research activities have been conducted to explore the phenomenon of thermochromism for decades, especially the reversible change of color with temperature [1–3]. Recently, a variety of thermochromic materials such as vanadium dioxide [4], hydrogels [5], polymers [6], synthetic dyes [7], organic crystals [8] and coordination compounds [9] are synthesized and studied. Moreover, the organic-inorganic hybrid compounds have been extensively studied for their structure property relationships as new thermochromic materials [10,11]. In these hybrid compounds, the presence of inorganic components provides excellent electronic properties as well as mechanical and thermal stability, while the organic components ensure structural flexibility and synthetic versatility [12,13]. In addition, the changes in coordination geometry, breaking and formation of bonds, dynamic structure changes, charge transfer and coordination ligand patterns [14] could give rise to reversible thermochromic properties.

Among the organic-inorganic metal halide hybrids, the lead-based hybrids show superior properties including high charge-carrying mobility [15], structural flexibility for optical bandgap tuning [16], long diffusion length [17], and low-cost solution preparation [18], thus attracted wide-spread interest in their properties and applications. However, water-soluble Pb^{2+} has high toxicity and can contaminate groundwater during processing, which is harmful and not sustainable [19]. The toxicity of lead can be eliminated /reduced by replacing lead with less toxic elements, such as tin (Sn) [20,21], germanium (Ge) [22], copper (Cu) [23], bismuth (Bi) [24,25] and antimony (Sb) [26,27]. Among these elements, bismuth (Bi) and antimony (Sb) have already attracted the attention of researchers for their unique properties [28,29]. In addition to their environmental friendliness, they also exhibit long-term phase stability [30] and significant photoelectric properties [31,32]. Therefore, incorporating Bi^{3+} and Sb^{3+} into organic-inorganic hybrids may result in many further benefits.

* Corresponding authors.
E-mail addresses: shouyu.wang@yahoo.com (S.Y. Wang), wfliu@tju.edu.cn (W.F. Liu).

https://doi.org/10.1016/j.jallcom.2021.163278
0925-8388/

Recently an interesting material, in which the organic cations are separated from the metal halide polyhedrons (thus was called a zero-dimensional structure in molecular size), has drawn considerable attention [33–35]. These zero-dimension materials have been reported to have superior stability as compared to those with high dimensional metal halide organic-inorganic hybrid backbone, which can easily collapse [36–38]. Moreover, high-dimensional metal halide organic-inorganic hybrids often limit the extent of local structural flexibility, thus placing high structural requirements for cations, which in turn limits the potential developments of new organic-inorganic metal halide hybrids. In contrast, 0D hybrid organic-inorganic metal halide hybrids have large organic cations and large interstitial spaces, therefore allowing for considerable excited state structural relaxation.

In this paper, we successfully synthesized the quasi 0D lead-free organic-inorganic hybrid single crystals: $(C_7H_9NF)_8M_4I_{16}$ (M = Bi, Sb) by using a conventional solvothermal reaction method; we also provided a detailed structural description. In $(C_7H_9NF)_8M_4I_{16}$ (M = Bi, Sb), the organic functional group separates the inorganic clusters and form a zero-dimensional structure. An interesting reversible thermochromic behavior was observed. Through AIMD simulations, the temperature dependence of the structure and optical properties of $(C_7H_9NF)_8M_4I_{16}$ (M = Bi, Sb) were analyzed. Results suggest that the reversible thermochromic behavior is likely related to the bandgap changes.

2. Experimental section and computational method

Hybrid organic-inorganic $(C_7H_9NF)_8M_4I_{16}$ (M = Bi, Sb) single crystals with 0D monoclinic structure were synthesized by using the solvothermal reaction method. Single crystal diffraction intensity data of $(C_7H_9NF)_8M_4I_{16}$ (M = Bi, Sb) were collected by a Bruker APEX-II CCD diffractometer[1] equipped with graphite monochromatic Mo-Kα radiation. The radiation wavelength was 0.71073 Å, and the φ-ω scan technique was used at ambient temperature. No crystal decay was found during the data collection period. Through the semi-empirical absorption correction (SADABS), the program SAINT was used to integrate the diffraction curves. The structure was solved by the direct method, and the SHELXL-2014 program was used for refinement by the full matrix least square method. The anisotropic thermal parameter was assigned to all non-hydrogen atoms. The crystalline structure analysis of the samples was recorded by X-ray diffraction (XRD, D/Max-2500 diffractometer with Cu Kα radiation; Rigaku Co., Tokyo, Japan). Rietveld refinements of samples were carried out using the FULLPROF package. Germany). UV vis absorption spectra were recorded with a UV 3600UV VIS NIR spectrophotometer (Shimadzu Co., Tokyo, Japan). First The valence band spectrum was analyzed by X-ray photoelectron spectroscopy (XPS) with PHI1600 (U1vac-Phi Co., Chigasaki, Kanagawa, Japan).

Synthesis of $(C_7H_9NF)_8M_4I_{16}$ (M = Bi, Sb) single crystals. The BiI_3 (0.5 mmol) was first dissolved in HI (0.5 ml), and 2-F-3.5-dimethylimidazole (1.0 mmol) was also dissolved in methanol (10.0 ml) respectively. The two solutions were mixed into a Teflon-lined autoclave and heated in a programmable oven with the following parameters: 6 h heating from room temperature to 180 °C, 24–30 h remaining at 180–185 °C, and then cooling down to room temperature with 15 °C /h. Finally, red crystals of $(C_7H_9NF)_8Bi_4I_{16}$ and the yellow crystals $(C_7H_9NF)_8Sb_4I_{16}$ were obtained by filtration and methanol washing.

Computational Details: First-principles calculations were performed by the density function theory (DFT) method implemented in the Vienna Ab initio Simulation Package (VASP) [39–42]. The projector augmented wave method with a plane wave energy cutoff at 500 eV and the energy convergence of electric structures of $< 10^{-5}$ eV were used. In order to accurately estimate the bandgap of the systems, the exchange-correlation energy was described by a generalized gradient approximation (GGA) with Heyde-Scuseriae-Ernzerhof (HSE06) hybrid functional [43,44]. The calculated mode was optimized with a *k*-points sampling of 1 × 1 × 1 for the 328 atoms of $(C_7H_9NF)_8M_4I_{16}$ (M = Bi, Sb). *Ab initio* molecular dynamics (AIMD) simulations with NVT ensemble was used to calculate the structure at finite temperature [45]. The running time of the AIMD simulation was 15 ps with a time step of 3 fs, and the Γ point sampling in the Brillouin zone was applied. In order to explicitly investigate effects of thermal vibrations on the electronic properties, calculations were performed for the experimental lattice constants of $(C_7H_9NF)_8M_4I_{16}$ (M = Bi, Sb) at 100 °C and 150 °C.

3. Result and discussion

Crystallographic data of the $(C_7H_9NF)_8M_4I_{16}$ (M = Bi, Sb) single crystals were presented in Table 1 and as supplement materials (Tables S1–S7). Both the $(C_7H_9NF)_8M_4I_{16}$ (M = Bi, Sb) compounds have a monoclinic structure with a space group of $P2_1/n$. The cell parameters are shown in Table 1. Fig. 1 depicts the crystal structure of $(C_7H_9NF)_8M_4I_{16}$ (M = Bi, Sb) viewing from the directions of *a, b* and *c*, respectively. It is clear that the organic cations separate metal halide polyhedrons from each other, resulting in a zero-dimensional structure in molecular size. Due to the large size of the organic cations, the 0D organic-inorganic hybrids have significant structural tunability and diversity. It can be seen from Fig. 1(d) that the inorganic anion moiety is comprised of corner-sharing $[MI_6]^{3-}$ octahedra in which the central bismuth atom is coordinated with six iodine atoms. The M-I bond lengths of $[M_4I_{16}]$ (Tables S3 and S4) reflect the distortion of the two independent octahedrons of $(C_7H_9NF)_8M_4I_{16}$. As a result, the inorganic tetranuclear cluster adopts a highly distorted $[M_4I_{16}]$ motif. In Tables S3 and S4, the subtle differences in the structure between $(C_7H_9NF)_8Bi_4I_{16}$ and $(C_7H_9NF)_8Sb_4I_{16}$ are noted. The Bi-I bonds are slightly longer than the corresponding Sb-I bonds, and the I-Bi-I bond angles are mostly smaller than the corresponding I-Sb-I bond angles.

The $(C_7H_9NF)_8M_4I_{16}$ (M = Bi, Sb) single crystals have different morphologies, needle-like for $(C_7H_9NF)_8Bi_4I_{16}$ and blocky-shaped for $(C_7H_9NF)_8Sb_4I_{16}$. As shown in Fig. 2(a), the powder XRD pattern is consistent with the simulated pattern derived from the single crystal structure data. Besides, through the Rietveld refinements, the diffraction pattern and the calculated pattern matched well, which further confirmed that they are pure phases (Fig. 2(b)). It is worth noting that by measuring the powder XRD of $(C_7H_9NF)_8M_4I_{16}$ (M = Bi, Sb) after exposure to the ambient atmosphere for 30, 60, and 90 days, no additional peaks appear (Figs. 2(c) and S1(a)), which indicates its outstanding stability in air. The powder XRD patterns of $(C_7H_9NF)_8Sb_4I_{16}$ have similar properties as that of $(C_7H_9NF)_8Bi_4I_{16}$, and the relevant results are shown in the supplementary material (Fig. S1). Fig. 2(d) shows the enlarged views of the diffraction peaks located at about 26–28.5° for $(C_7H_9NF)_8Bi_4I_{16}$ and $(C_7H_9NF)_8Sb_4I_{16}$. It can be seen that the (4,0,0) peak of $(C_7H_9NF)_8Bi_4I_{16}$ is shifted to the higher 2θ region as compared with that in $(C_7H_9NF)_8Sb_4I_{16}$, which is consistent with the larger lattice parameter '*a*' of $(C_7H_9NF)_8Sb_4I_{16}$.

Materials with high thermal stability often have important industrial applications in various high-temperature fields, including aerospace, automobile engines, and ship engines, etc. To explore the origins of their thermal stability, we conducted thermal gravimetric analyses. From the shape of these thermogravimetric curves (Fig. S2), it is clear that the $(C_7H_9NF)_8M_4I_{16}$ (M = Bi, Sb) compounds begin to decompose at about 200 °C, and $(C_7H_9NF)_8Bi_4I_{16}$ decomposed more slowly than $(C_7H_9NF)_8Sb_4I_{16}$. $(C_7H_9NF)_8Sb_4I_{16}$ was completely

[1] The purpose of identifying the equipment and software in this article is to specify the experimental procedure. Such identification does not imply recommendation or endorsement by the National Institute of Standards and Technology.

Table 1
Crystal data and structure refinement for $(C_7H_9NF)_8M_4I_{16}$ (M = Bi, Sb).

Empirical formula	$C_{28}H_{36}Bi_2F_4I_8N_4$	$C_{28}H_{36}F_4I_8N_4Sb_2$
Formula weight	1937.77	1763.31
Temperature/K	296.15	296.15
Crystal system	monoclinic	monoclinic
Space group	$P2_1/n$	$P2_1/n$
a/Å	14.187(7)	14.221(2)
b/Å	16.876(8)	16.810(3)
c/Å	20.479(10)	20.579(3)
α/°	90	90
β/°	108.846(10)	108.952(3)
γ/°	90	90
V (Volume/Å^3)	4640(4)	4652.9(13)
Z	4	4
ρ_{calc}g/cm^3	2.774	2.517
μ/mm^{-1}	12.936	6.509
F(000)	3432.0	3176.0
Crystal size/mm^3	0.22 × 0.21 × 0.18	0.22 × 0.21 × 0.18
Radiation (Å)	MoKα (λ = 0.71073)	MoKα (λ = 0.71073)
2θ range for data collection/°	3.082–53	3.072–52.994
Index ranges	-15 ≤ h ≤ 17, − 21 ≤ k ≤ 18, − 25 ≤ l ≤ 23	-15 ≤ h ≤ 17, − 21 ≤ k ≤ 19, − 25 ≤ l ≤ 25
Reflections collected	30135	29266
Independent reflections	9614 [R_{int} = 0.0829, R_{sigma} = 0.0839]	9632 [R_{int} = 0.0785, R_{sigma} = 0.0967]
Data/restraints/ parameters	9614/0/415	9632/0/415
Goodness-of-fit on F^2	1.016	1.035
Final R indexes [I > =2σ (I)]	R_1 = 0.0461, wR_2 = 0.0729	R_1 = 0.0768, wR_2 = 0.2028
Final R indexes [all data]	R_1 = 0.0932, wR_2 = 0.0802	R_1 = 0.0970, wR_2 = 0.2172
Largest diff. peak/ hole / e Å^3	1.38/− 1.60	2.57/− 3.27

decomposed at around 300 °C, while $(C_7H_9NF)_8Bi_4I_{16}$ still remained until 380 °C. These results show that $(C_7H_9NF)_8M_4I_{16}$ (M = Bi, Sb) have excellent thermal stability. At the same time, we found that the color of $(C_7H_9NF)_8Bi_4I_{16}$ and $(C_7H_9NF)_8Sb_4I_{16}$ changes during heating. The optical images of these compounds from room temperature to 200 °C are illustrated in Fig. 3(a) and (b). It can be clearly observed that both samples undergo thermochromic changes at elevated temperatures. Initially, $(C_7H_9NF)_8Bi_4I_{16}$ and $(C_7H_9NF)_8Sb_4I_{16}$ exhibited red and yellow color respectively at room temperature. As the temperature rises from RT to 200 °C, the color of $(C_7H_9NF)_8Bi_4I_{16}$ gradually darkens from red and finally becomes black, and the color of $(C_7H_9NF)_8Sb_4I_{16}$ also gradually darkens (changes from yellow to red and darkens further). Interestingly, when the temperature returns to room temperature, the color for both $(C_7H_9NF)_8Bi_4I_{16}$ and $(C_7H_9NF)_8Sb_4I_{16}$ returns to their original state (Fig. 3), indicating that $(C_7H_9NF)_8Bi_4I_{16}$ and $(C_7H_9NF)_8Sb_4I_{16}$ exhibit fully reversible thermochromic behavior. To explore this reversible thermochromic phenomenon further, UV absorption spectra of $(C_7H_9NF)_8Bi_4I_{16}$ and $(C_7H_9NF)_8Sb_4I_{16}$ at different temperatures were examined, as shown in Fig. 4.

Fig. 4(a) and (c) show the ultraviolet–visible-near-infrared (UV–vis–NIR) absorption spectra for $(C_7H_9NF)_8M_4I_{16}$ (M = Bi, Sb) at RT, 50 °C, 100 °C and 150 °C. As shown in the absorbance plot, the intrinsic absorption of the $(C_7H_9NF)_8Bi_4I_{16}$ and $(C_7H_9NF)_8Sb_4I_{16}$ samples at room temperature appears at 640 nm and 588 nm respectively. Besides the main intrinsic absorption, there are small absorption peaks in the energy region above the band edge as shown in Fig. S3(a) and (b), which are attributed to the organic part of the samples. All these absorption peaks are marked, they are all due to the electronic transition of π-π* [46,47]. As can be seen from Fig. S3(a) and (b), these types of absorption are very weak compared with the intrinsic absorption. Thus, in the following discussion, we are mainly concerned with the intrinsic absorption of $(C_7H_9NF)_8M_4I_{16}$ (M = Bi, Sb). As the temperature increases from RT to

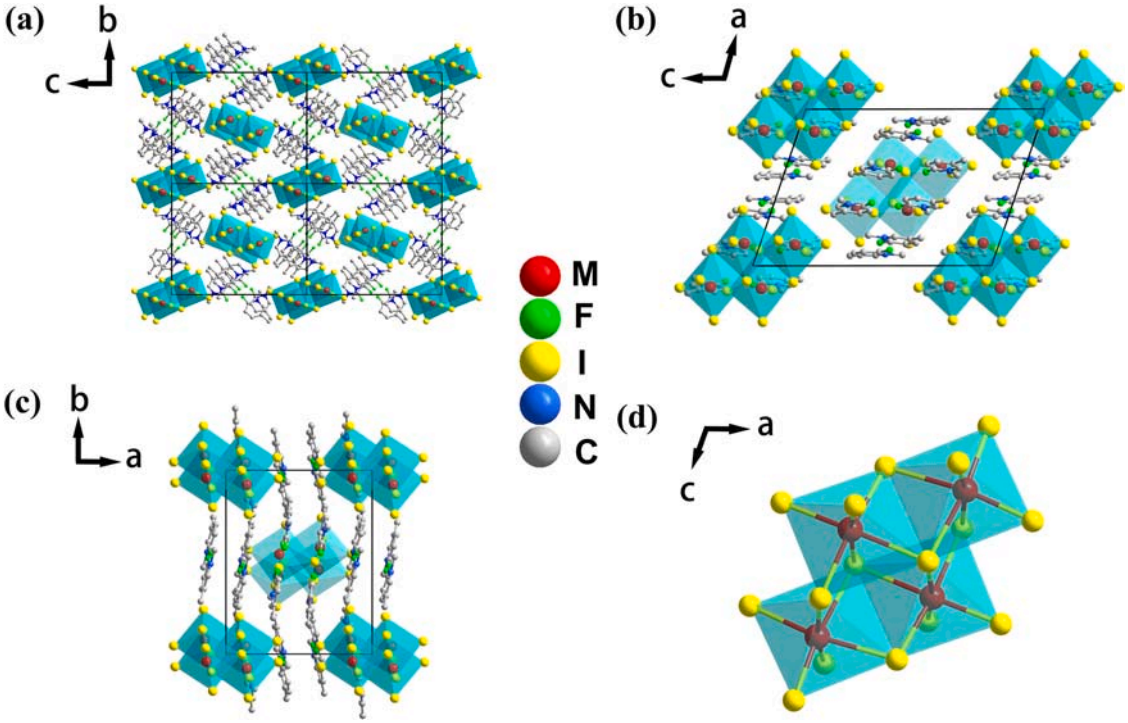

Fig. 1. **(a)** The supercell structure of $(C_7H_9NF)_8M_4I_{16}$ (M = Bi, Sb) view from the directions of *a*. **(b-c)** The crystal structure of $(C_7H_9NF)_8M_4I_{16}$ (M = Bi, Sb) view from the directions of *b* and *c*. **(d)** The inorganic tetranuclear cluster of $(C_7H_9NF)_8M_4I_{16}$ (M = Bi, Sb).

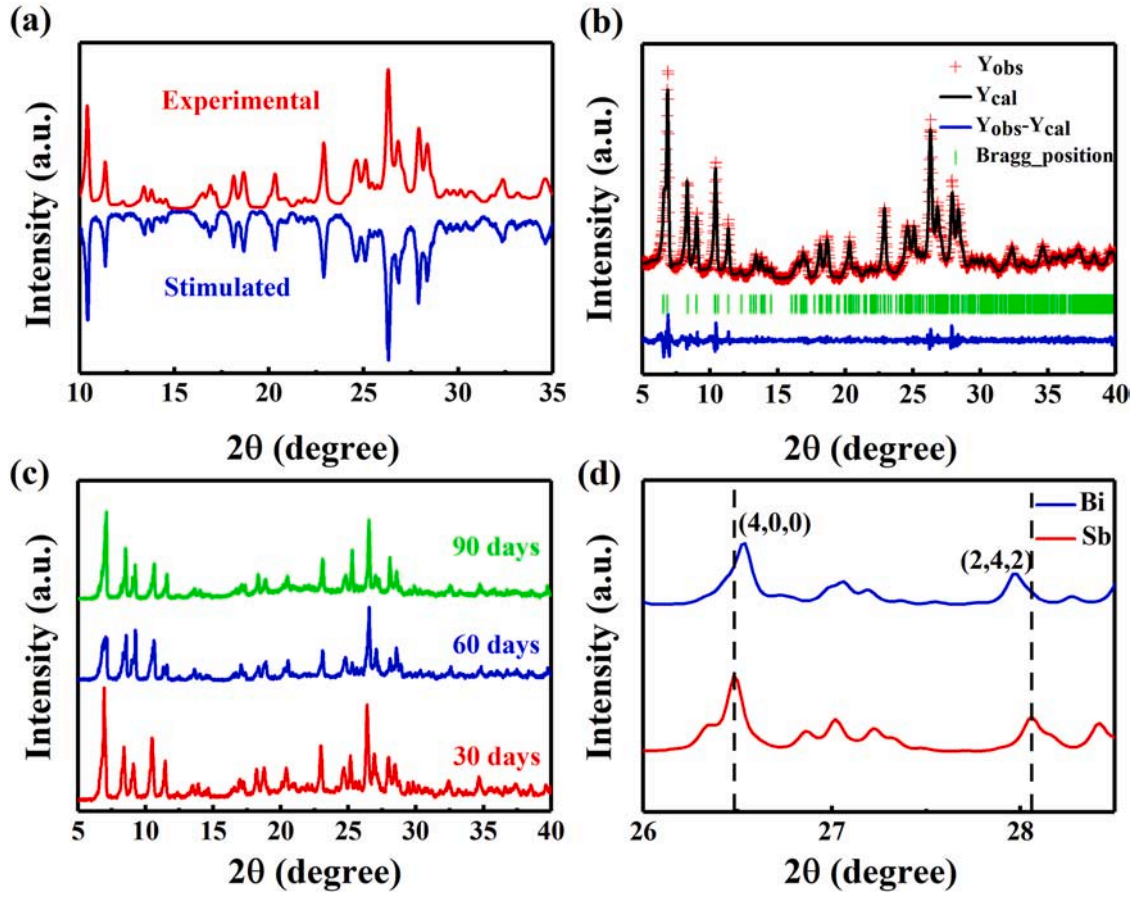

Fig. 2. **(a)** Comparison of the experimental and theoretical XRD of $(C_7H_9NF)_8Bi_4I_{16}$. **(b)**Refinement results of the XRD of $(C_7H_9NF)_8Bi_4I_{16}$ using FULLPROF package. **(c)** The XRD of $(C_7H_9NF)_8Bi_4I_{16}$ single crystals after exposed to air for 30 days, 60 days, and 90 days. **(d)** Enlarge views of the diffraction peaks located at about 26–28.5° for $(C_7H_9NF)_8Bi_4I_{16}$ and $(C_7H_9NF)_8Sb_4I_{16}$.

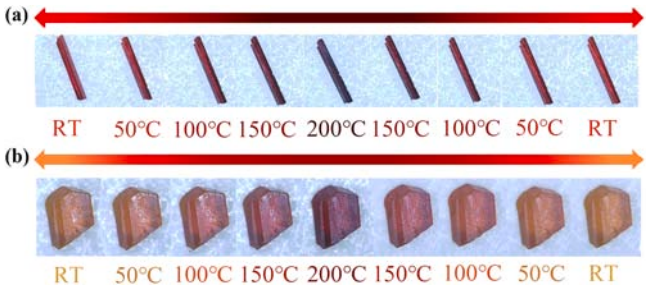

Fig. 3. **(a-b)** Optical images of $(C_7H_9NF)_8Bi_4I_{16}$ and $(C_7H_9NF)_8Sb_4I_{16}$, respectively, at different temperatures for one heating–cooling cycle.

200 °C, the absorption edges of $(C_7H_9NF)_8Bi_4I_{16}$ and $(C_7H_9NF)_8Sb_4I_{16}$ show a gradual red shift. The bandgap can be calculated using the following formula (Tauc plot method) [48]:

$$F(R) = \frac{(1-R)^2}{2R}$$

$$[F(R)h\nu]^{1/n} = A(h\nu - E_g)$$

In this formula, R, $h\nu$, and E_g represent the percentage of reflection, light energy, and bandgap energy, respectively, while A and n are constants, (n = 0.5 for direct bandgap materials, and n = 2 for indirect bandgap materials). To determine the correct extrapolation formula, the type of bandgap should be calculated first. The band structure and density of states (DOS) were calculated for $(C_7H_9NF)_8M_4I_{16}$ (M = Bi, Sb) using density functional theory (DFT) [41,42]. As shown in Fig. 5(c) and (d), $(C_7H_9NF)_8M_4I_{16}$ (M = Bi, Sb) have nearly flat conduction band and valence band, because the large organic cations in the hybrid organic inorganic halides reduce the electronic coupling among the inorganic MI_6 octahedra [38]. The almost flat conduction band and valence band can be considered as a direct bandgap. Therefore, the bandgaps E_g of $(C_7H_9NF)_8M_4I_{16}$ (M = Bi, Sb) were determined using the following formula: $[F(R)h\nu]^2 = A(h\nu - E_g)$.

The inset in Fig. 4(a) and (c) show the Tauc plots of the absorption spectrum of $(C_7H_9NF)_8M_4I_{16}$ (M = Bi, Sb) for various temperatures. The bandgaps obtained by linear extrapolation were found to be approximately 2.34 eV and 2.1 eV at RT for $(C_7H_9NF)_8Sb_4I_{16}$ and $(C_7H_9NF)_8Bi_4I_{16}$ respectively. As the temperature rises, the bandgaps gradually decrease. In order to further analyze the bandgap values, the valence band spectra were analyzed by X-ray photoelectron spectroscopy (XPS). In Fig. 4(b) and (d), the valence bandgap of $(C_7H_9NF)_8Sb_4I_{16}$ and $(C_7H_9NF)_8Bi_4I_{16}$ were estimated to be 1.53 eV and 1.52 eV respectively. Combined with the bandgap values of $(C_7H_9NF)_8Sb_4I_{16}$ and $(C_7H_9NF)_8Bi_4I_{16}$, it indicates both Fermi levels are located close to the conduction band, as shown in the inset of Fig. 4(b) and (d). Thus, the crystals have the properties of N-type semiconductors, which implies that both $(C_7H_9NF)_8Sb_4I_{16}$ and

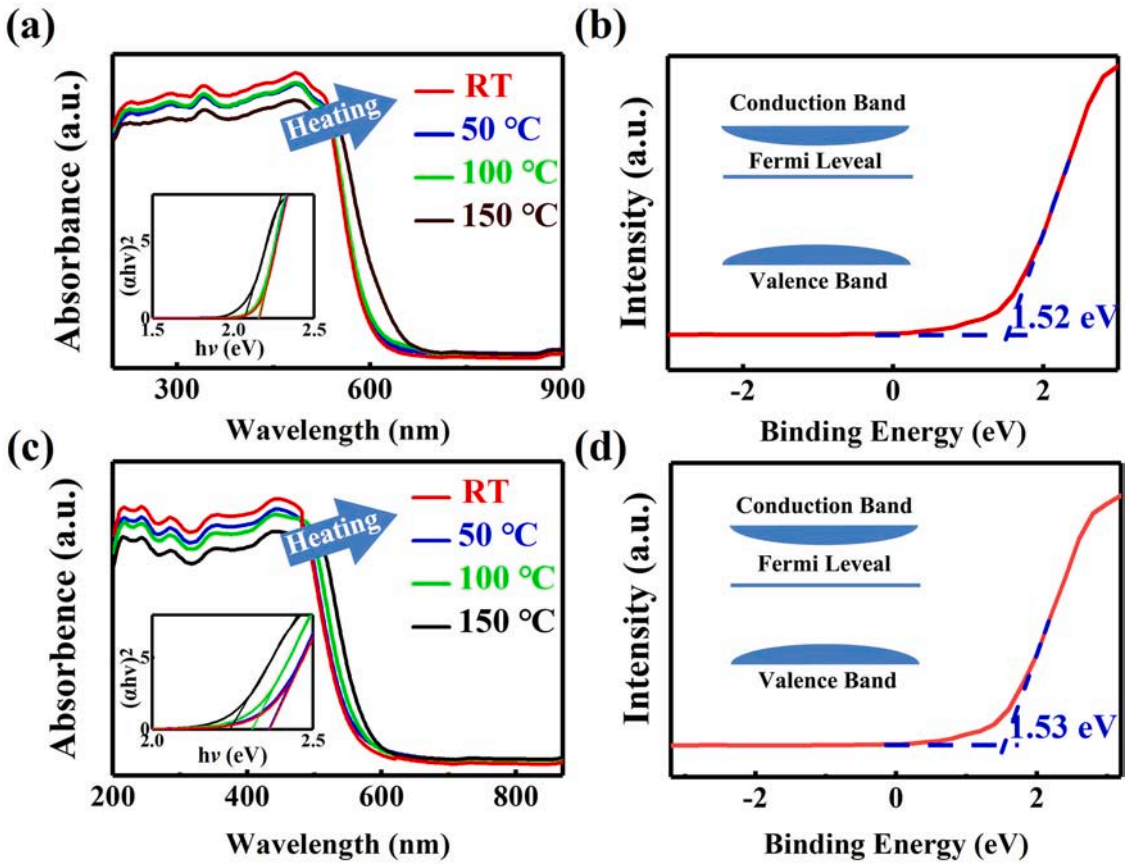

Fig. 4. **(a)** Optical diffuse reflectance spectra for $(C_7H_9NF)_8Bi_4I_{16}$. The inset shows their bandgaps deduced from the Tauc plot. **(b)** Valence band spectrum for $(C_7H_9NF)_8Bi_4I_{16}$. **(c)** Optical diffuse reflectance spectra for $(C_7H_9NF)_8Sb_4I_{16}$. **(d)** Valence band spectrum for $(C_7H_9NF)_8Sb_4I_{16}$.

$(C_7H_9NF)_8Bi_4I_{16}$ are multi-electron system materials. To analyze in detail their electronic structure, the density of states (DOS) was calculated as shown in Fig. 5(a) and (b). The bandgaps estimated here are somewhat smaller than those deduced from experiments, which is expected because it is known that the DFT approach often underestimate the values of bandgap. In addition, to further understand the distribution of the bandgap in $(C_7H_9NF)_8M_4I_{16}$ (M = Bi, Sb), partial projected density of states (PDOS) were also analyzed and shown in Fig. 6. Obviously, the H-1*s* state, the N-2*s*2*p* state and the C-2*s*2*p* state overlap in the energy range of − 10 to + 10 eV, which is consistent with the pyridine ring of the organic functional group. The PDOS also shows that the conduction band (CB) of $(C_7H_9NF)_8Bi_4I_{16}$ is mainly dominated by the C-2*p* state and N-2*p* state, while valence band (VB) is mainly contributed by the Bi-6*s* state and I-5*s*5*p* state. For $(C_7H_9NF)_8Sb_4I_{16}$ the CB is also mainly dominated by the C-2*p* state and N-2*p* state, and VB is mainly dominated by Sb-5*s* state and I-5*s*5*p* state (Fig. 6(a) and (b)). It is worth noting that the$(C_7H_9NF)_8M_4I_{16}$ (M = Bi, Sb) compounds are unlike most of the organic–inorganic hybrids, whose bandgaps are determined only by the inorganic moieties [49–51]. In $(C_7H_9NF)_8M_4I_{16}$ (M = Bi, Sb), both inorganic moieties and organic moieties contribute to the bandgaps.

To better explore the causes of thermal discoloration, taking $(C_7H_9NF)_8Sb_4I_{16}$ as an example, we conducted an *ab Initio* Molecular Dynamics (AIMD) simulation, which can provide an atomic-level description of temperature-dependent material structure properties. In Fig. 7, density of states at 100 °C and 150 °C were calculated by AIMD simulations, the bandgaps of $(C_7H_9NF)_8Sb_4I_{16}$ were estimated to be 2.14 and 2.01 eV at 100 and 150 °C, respectively. Compared with the experimental results, although the bandgap is underestimated, it is consistent with the trend of the bandgap reduction at higher temperatures. The partial projected density of states (PDOS) and HOMO (highest occupied molecular orbital) and LUMO (lowest unoccupied molecular orbital) of $(C_7H_9NF)_8Sb_4I_{16}$ at RT, 100 °C and 150 °C were simulated and results were presented in Fig. 7 and Fig. 8. With the increase of temperature, the HOMO and LUMO change significantly. As the temperature increases, the electron density of the inorganic clusters decreases, while the electron density of the organic functional groups increases significantly. Based on these results, it is conjectured that an electronic transition occurs between the inorganic clusters and the organic functional groups. The increase in electron density of organic functional groups enables the electron orbits of adjacent organic functional groups overlap to a greater extent at elevated temperatures (which can be attributed to the thermal excitation of electrons at higher temperatures). From Fig. 7, the energy range in CB becomes larger in 150 °C compared with that at 100 °C, which in turn confirmed that electrons are more energetic at high temperatures. As the electrons become more energetic as the temperature increases, the transition of electrons between inorganic clusters and organic functional groups intensifies, leading to a reduction in the bandgap. Accordingly, the absorption edge will have a red shift tendency in the heating process from RT to 100–150 °C, which is consistent with the experimental variable-temperature UV–vis absorption spectra, and in turn leads to the occurrence of thermochromism.

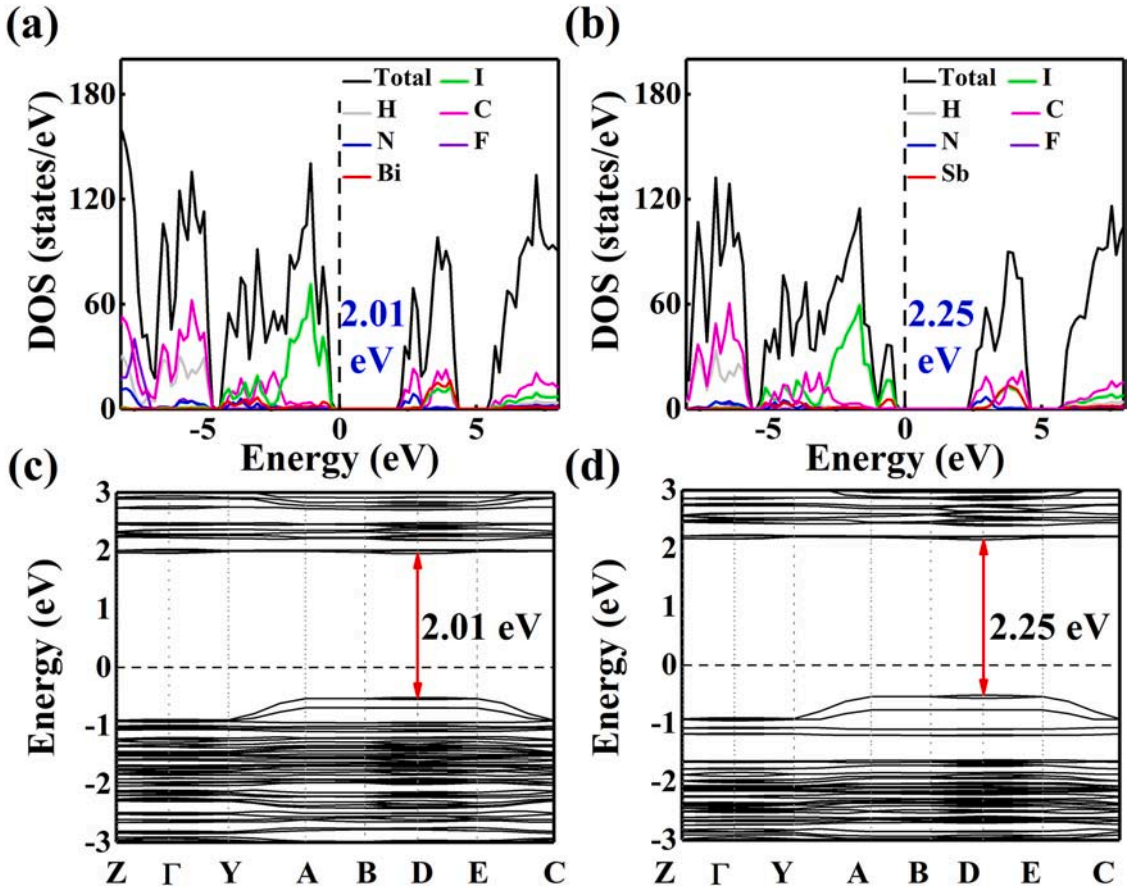

Fig. 5. **(a-b)** Density of states of $(C_7H_9NF)_8M_4I_{16}$ (M = Bi, Sb). **(c-d)** Band structure diagrams of $(C_7H_9NF)_8M_4I_{16}$ (M = Bi, Sb).

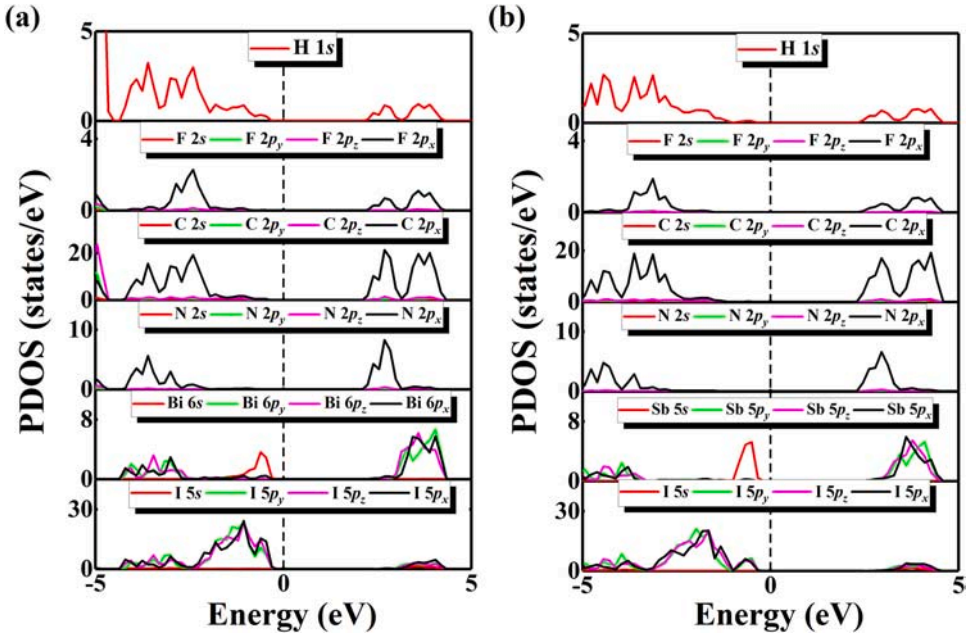

Fig. 6. The atomic projected DOS of **(a)** $(C_7H_9NF)_8Bi_4I_{16}$ and **(b)** $(C_7H_9NF)_8Sb_4I_{16}$.

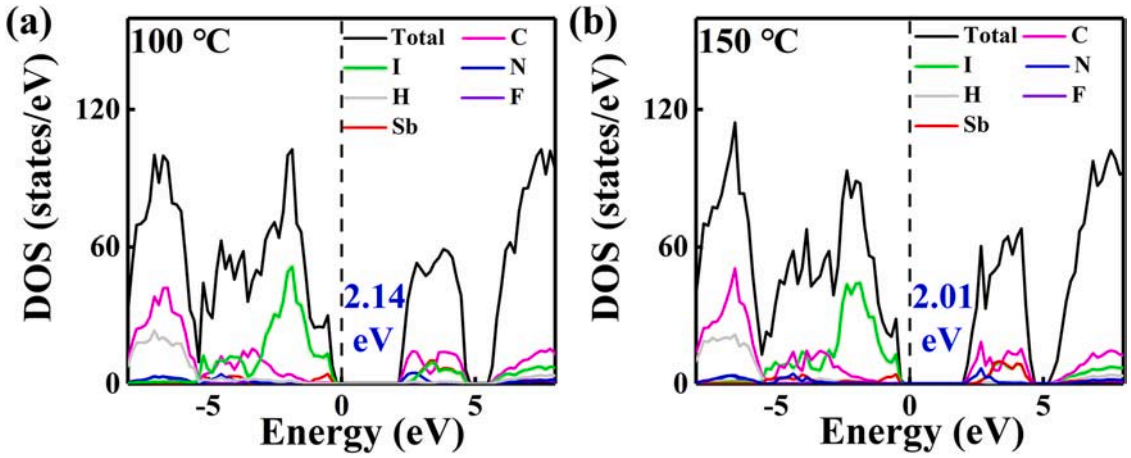

Fig. 7. Density of states of $(C_7H_9NF)_8Sb_4I_{16}$ at 100 °C and 150 °C by ab initio Molecular Dynamics (AIMD) simulation.

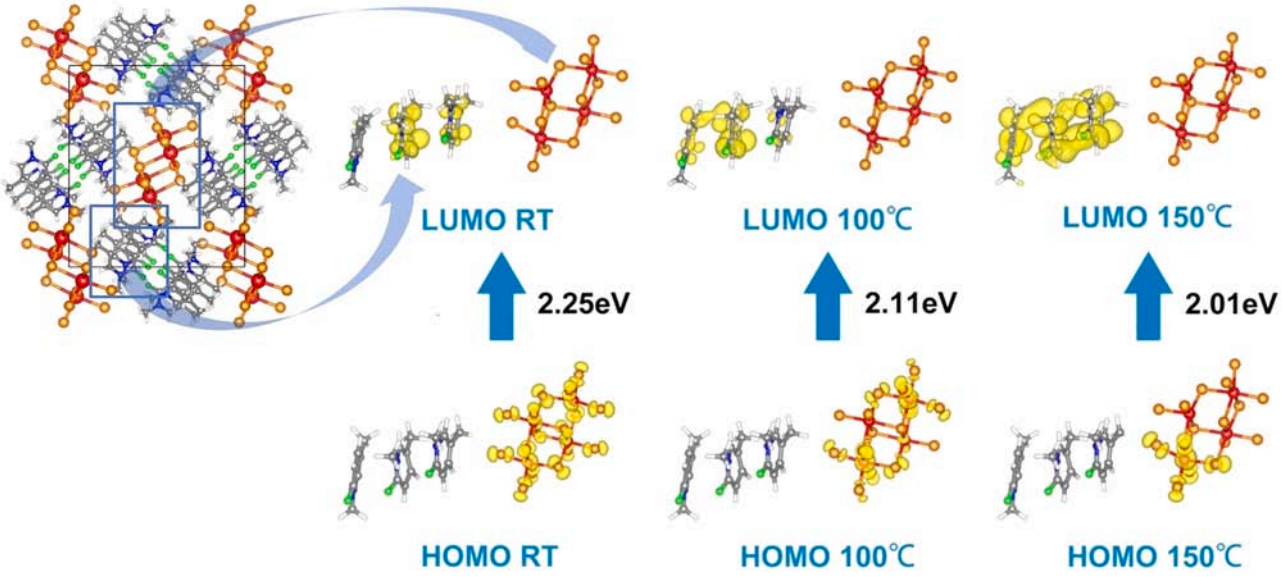

Fig. 8. Schematics of simulated HOMO-LUMO transitions for $(C_7H_9NF)_8Sb_4I_{16}$ (M = Bi, Sb) at RT, 100 °C and 150 °C.

4. Conclusions

In summary, the quasi-0D lead-free organic-inorganic hybrid compounds $(C_7H_9NF)_8M_4I_{16}$ (M = Bi, Sb) were synthesized by a conventional solvothermal reaction method and a detailed structural description was given. These 0D hybrid organic-inorganic metal halide hybrids possess large organic cations and large interstitial space that allow for substantial excited-state structural relaxation. The $(C_7H_9NF)_8M_4I_{16}$ (M = Bi, Sb) samples exhibit outstanding reversible thermochromic properties. The band gap of $(C_7H_9NF)_8M_4I_{16}$ (M = Bi, Sb) decreases with increasing temperature. Through AIMD simulations, it can be inferred that electrons are thermally excited at higher temperatures. Thus, the occurrence of thermochromism is likely due to the electronic transitions between the organic functional groups and the inorganic clusters at high temperature, which resulted in the red shift of the electron absorption band.

CRediT authorship contribution statement

X.C. Zhao: Formal analysis, Investigation, Writing – original draft, Resources. **Y.K. Fu:** Formal analysis, Investigation. **Y.L. Lei:** Methodology. **Winnie Wong-Ng:** Writing – review & editing. **C. Wang:** Methodology. **Q. Gu**: Methodology. **W. Zhou:** Methodology. **S.Y. Wang:** Conceptualization, Formal analysis, Investigation. **W.F. Liu:** Supervision, Conceptualization, Methodology, Writing – review & editing.

Declaration of Competing Interest

The authors declare that they have no known competing financial interests or personal relationships that could have appeared to influence the work reported in this paper.

Acknowledgement

This work was funded by the National Natural Science Foundation of China (51572193), and Natural Science Foundation of Tianjin (20JCZDJC00210).

Appendix A. Supporting information

Supplementary data associated with this article can be found in the online version at doi:10.1016/j.jallcom.2021.163278.

References

[1] J. Pitchaimani, S. Karthikeyan, N. Lakshminarasimhan, S.P. Anthony, D. Moon, V. Madhu, Reversible thermochromism of nickel(II) complexes and single-crystal-to-single-crystal transformation, ACS Omega 4 (2019) 13756–13761.

[2] H. Wei, J. Gu, F. Ren, L. Zhang, G. Xu, B. Wang, S. Song, J. Zhao, S. Dou, Y. Li, Smart materials for dynamic thermal radiation regulation, Small 17 (2021) 2100446.

[3] J. Kim, T. Paik, Recent advances in fabrication of flexible, thermochromic vanadium dioxide films for smart windows, Nanomaterials 11 (2021) 2674.

[4] S. Guan, M. Souquet-Basiège, O. Toulemonde, D. Denux, N. Penin, M. Gaudon, A. Rougier, Toward room-temperature thermochromism of VO_2 by Nb doping: magnetic investigations, Chem. Mater. 31 (2019) 9819–9830.

[5] M. Nakamitsu, H. Imai, Y. Oaki, Visualization and quantification of microwaves using thermoresponsive color-change hydrogel, ACS Sens. 5 (2020) 133–139.

[6] D.A. Turchetti, A.J. Santana, L.G.T.A. Duarte, T.D.Z. Atvars, R.A. Domingues, L. Akcelrud, Ratiometric thermochromism in europium-containing conjugated polymer, Polymer 177 (2019) 65–72.

[7] W. Zhang, X. Ji, B.J. Peng, S. Che, F. Ge, W. Liu, M. Al-Hashimi, C. Wang, L. Fang, High-performance thermoresponsive dual-output dye system for smart textile application, Adv. Funct. Mater. 30 (2020) 1906463.

[8] W. Zhang, X. Ji, K. Chen, C. Wang, S. Sun, Thermochromic performance of a new temperature sensitive pigment based on rhodamine derivative in both liquid and solid systems, Prog. Org. Coat. 137 (2019) 105280.

[9] O. Shakirova, A. Protsenko, A. Protsenko, N. Kuratieva, S. Fowles, M.M. Turnbull, Syntheses, structures and properties of copper(II) and cobalt(II) complexes with 5(3)-amino-2-chloro-3(5)-methylpyridine isomer cations, Inorg. Chim. Acta 500 (2020) 119246.

[10] H. Tong, H. Li, H. Li, F. Cidanpuchi, W. Wang, Liu, Incorporation of an emissive Cu_4I_4 Core into cross-linked networks: an effective strategy for luminescent organic-inorganic hybrid coatings, Inorg. Chem. 60 (2021) 15049–15054.

[11] Y.R. Huang, X.L. Lin, B. Chen, H.D. Zheng, Z.R. Chen, H.H. Li, S.T. Zheng, Thermal-responsive polyoxometalate-metalloviologen hybrid: reversible intermolecular three-component reaction and temperature-regulated resistive switching behaviors, Angew. Chem. Int. Ed. Engl. 60 (2021) 16911–16916.

[12] W.V. Taylor, C.X. Cammack, S.A. Shubert, M.J. Rose, Thermoluminescent antimony-supported copper-iodo cuboids: approaching NIR emission via high crystallographic symmetry, Inorg. Chem. 58 (2019) 16330–16345.

[13] Y. Zhang, C.Y. Tso, J.S. Iñigo, S. Liu, H. Miyazaki, C.Y.H. Chao, K.M. Yu, Perovskite thermochromic smart window: advanced optical properties and low transition temperature, Appl. Energy 254 (2019).

[14] L. Tom, M.R.P. Kurup, A stimuli responsive multifunctional ZMOF based on an unorthodox polytopic ligand: reversible thermochromism and anion triggered metallogelation, Dalton Trans. 48 (2019) 16604–16614.

[15] S.A. Veldhuis, P.P. Boix, N. Yantara, M. Li, T.C. Sum, N. Mathews, S.G. Mhaisalkar, Perovskite materials for light-emitting diodes and lasers, Adv. Mater. 28 (2016) 6804–6834.

[16] M.J. Islam, M. Shahjahan, Ki Yuyama, V. Biju, Remote tuning of bandgap and emission of lead perovskites by spatially controlled halide exchange reactions, ACS Mater. Lett. 2 (2020) 403–408.

[17] Q.F. Dong, J. Qiu, Y.J. Fang, L. Cao, Y.C. Shao, Padhraic Jinsong Huang, Electron-hole diffusion lengths > 175 μm in solution-grown $CH_3NH_3PbI_3$ single crystals, Science 347 (2015) 967–970.

[18] R. Chen, Z. Cheng, Y. Hu, L. Jiang, P. Pan, J. Mao, C. Ni, Discarded clothing acrylic yarns: low-cost raw materials for deformable c nanofibers applied to flexible sodium-ion batteries, Electrochim. Acta 359 (2020).

[19] Y. Jiang, L. Qiu, E.J. Juarez-Perez, L.K. Ono, Z. Hu, Z. Liu, Z. Wu, L. Meng, Q. Wang, Y. Qi, Reduction of lead leakage from damaged lead halide perovskite solar modules using self-healing polymer-based encapsulation, Nat. Energy 4 (2019) 585–593.

[20] M. Konstantakou, T. Stergiopoulos, A critical review on tin halide perovskite solar cells, J. Mater. Chem. A 5 (2017) 11518–11549.

[21] T.M. Koh, T. Krishnamoorthy, N. Yantara, C. Shi, W.L. Leong, P.P. Boix, A.C. Grimsdale, S.G. Mhaisalkar, N. Mathews, Formamidinium tin-based perovskite with low E_g for photovoltaic applications, J. Mater. Chem. A 3 (2015) 14996–15000.

[22] T. Krishnamoorthy, H. Ding, C. Yan, W.L. Leong, T. Baikie, Z. Zhang, M. Sherburne, S. Li, M. Asta, N. Mathews, S.G. Mhaisalkar, Lead-free germanium iodide perovskite materials for photovoltaic applications, J. Mater. Chem. A 3 (2015) 23829–23832.

[23] D. Cortecchia, H.A. Dewi, J. Yin, A. Bruno, S. Chen, T. Baikie, P.P. Boix, M. Gratzel, S. Mhaisalkar, C. Soci, N. Mathews, Lead-free $MA_2CuCl_xBr_{4-x}$ hybrid perovskites, Inorg. Chem. 55 (2016) 1044–1052.

[24] A.H. Slavney, T. Hu, A.M. Lindenberg, H.I. Karunadasa, A. Bismuth-Halide, Double perovskite with long carrier recombination lifetime for photovoltaic applications, J. Am. Chem. Soc. 138 (2016) 2138–2141.

[25] M.B. Johansson, H. Zhu, E.M. Johansson, Extended photo-conversion spectrum in low-toxic Bismuth halide perovskite solar cells, J. Phys. Chem. Lett. 7 (2016) 3467–3471.

[26] B. Saparov, F. Hong, J.P. Sun, H.S. Duan, W. Meng, S. Cameron, I.G. Hill, Y. Yan, D.B. Mitzi, Thin-film preparation and characterization of $Cs_3Sb_2I_9$: a lead-free layered perovskite semiconductor, Chem. Mater. 27 (2015) 5622–5632.

[27] K.M. Boopathi, P. Karuppuswamy, A. Singh, C. Hanmandlu, L. Lin, S.A. Abbas, C.C. Chang, P.C. Wang, G. Li, C.W. Chu, Solution-processable antimony-based light-absorbing materials beyond lead halide perovskites, J. Mater. Chem. A 5 (2017) 20843–20850.

[28] B.W. Park, B. Philippe, X. Zhang, H. Rensmo, G. Boschloo, E.M. Johansson, Bismuth based hybrid perovskites $A_3Bi_2I_9$ (A: Methylammonium or Cesium) for solar cell application, Adv. Mater. 27 (2015) 6806–6813.

[29] Y.J. Li, T. Wu, L. Sun, R.X. Yang, L. Jiang, P.F. Cheng, Q.Q. Hao, T.J. Wang, R.F. Lu, W.Q. Deng, Lead-free and stable antimony-silver-halide double perovskite $(CH_3NH_3)_2AgSbI_6$, RSC Adv. 7 (2017) 35175–35180.

[30] B. Vargas, E. Ramos, E. Perez-Gutierrez, J.C. Alonso, D. Solis-Ibarra, A direct bandgap copper-antimony halide perovskite, J. Am. Chem. Soc. 139 (2017) 9116–9119.

[31] J.C. Hebig, I. Kühn, J. Flohre, T. Kirchartz, Optoelectronic properties of $(CH_3NH_3)_3Sb_2I_9$ thin films for photovoltaic applications, ACS Energy Lett. 1 (2016) 309–314.

[32] K.M. Boopathi, S. Raman, R. Mohanraman, F.C. Chou, Y.Y. Chen, C.H. Lee, F.C. Chang, C.W. Chu, Solution-processable bismuth iodide nanosheets as hole transport layers for organic solar cells, Sol. Energ. Mat. Sol. C 121 (2014) 35–41.

[33] B.A.H. Huisman, F. Palazon, H.J. Bolink, Zero-dimensional hybrid organic-inorganic lead halides and their post-synthesis reversible transformation into three-dimensional perovskites, Inorg. Chem. 60 (2021) 5212–5216.

[34] Q.Y. Pan, M.E. Sun, C. Zhang, L.K. Li, H.L. Liu, K.J. Li, H.Y. Li, S.Q. Zang, A multi-responsive indium-viologen hybrid with ultrafast-response photochromism and electrochromism, Chem. Commun. 57 (2021) 11394–11397.

[35] L. Han, P. Wang, Z. Wang, Y. Liu, Z. Zheng, H. Cheng, B. Huang, Zero-dimensional hydrazine iodobismuthate as a lead-free perovskite-like light absorber in a self-powered photodetector, J. Alloy. Comp. 893 (2022) 162347.

[36] C. Zhou, H. Lin, M. Worku, J. Neu, Y. Zhou, Y. Tian, S. Lee, P. Djurovich, T. Siegrist, B. Ma, Blue emitting single crystalline assembly of metal halide clusters, J. Am. Chem. Soc. 140 (2018) 13181–13184.

[37] C. Zhou, S. Lee, H. Lin, J. Neu, M. Chaaban, L.J. Xu, A. Arcidiacono, Q. He, M. Worku, L. Ledbetter, X. Lin, J.A. Schlueter, T. Siegrist, B. Ma, Bulk assembly of multi-component zero-dimensional metal halides with dual emission, ACS Mater. Lett. 2 (2020) 376–380.

[38] C. Zhou, H. Lin, Q. He, L. Xu, M. Worku, M. Chaaban, S. Lee, X. Shi, M.H. Du, B. Ma, Low dimensional metal halide perovskites and hybrids, Mat. Sci. Eng. R 137 (2019) 38–65.

[39] P.E. Blochl, Projector augmented-wave method, Phys. Rev. B 50 (1994) 17953–17979.

[40] G. Kresse, D. Joubert, From ultrasoft pseudopotentials to the projector augmented-wave method, Phys. Rev. B 59 (1999) 1758–1775.

[41] G. Kresse, J. Furthmüller, Efficiency of ab-initio total energy calculations for metals and semiconductors using a plane-wave basis set, Comp. Mater. Sci. 6 (1996) 15–50.

[42] G. Kresse, J. Furthmüller, Efficient iterative schemes for ab initio total-energy calculations using a plane-wave basis set, Phys. Rev. B 54 (1996) 11169–11186.

[43] J. Heyd, G.E. Scuseria, M. Ernzerhof, Assessment and validation of a screened Coulomb hybrid density functional, J. Chem. Phys. 120 (2004) 7274–7280.

[44] J. Heyd, J.E. Peralta, G.E. Scuseria, R.L. Martin, Energy band gaps and lattice parameters evaluated with the Heyd-Scuseria-Ernzerhof screened hybrid functional, J. Chem. Phys. 123 (2005) 174101.

[45] D. Bucher, L.C. Pierce, J.A. McCammon, P.R. Markwick, On the use of accelerated molecular dynamics to enhance configurational sampling in Ab initio simulations, J. Chem. Theory Comput. 7 (2011) 890–897.

[46] M.M. El-Nahass, A.A. Atta, H.E.A. El-Sayed, E.F.M. El-Zaidia, Structural and optical properties of thermal evaporated magnesium phthalocyanine (MgPc) thin films, Appl. Surf. Sci. 254 (2008) 2458–2465.

[47] M. Wojdyła, B. Derkowska, M. Rębarz, A. Bratkowski, W. Bała, Stationary and modulated absorption spectroscopy of copper phthalocyanine (CuPc) layers grown on transparent substrate, J. Opt. A Pure Appl. Opt. 7 (2005) 463–466.

[48] J. Tauc, R. Grigorovici, A. Vancu, Optical properties and electronic structure of amorphous germanium, Phys. Stat. Sol. 15 (1966) 627–637.

[49] Z. Wu, C. Ji, Z. Sun, S. Wang, S. Zhao, W. Zhang, L. Li, J. Luo, Broadband white-light emission with a high color rendering index in a two-dimensional organic-inorganic hybrid perovskite, J. Mater. Chem. C 6 (2018) 1171–1175.

[50] C. Ji, P. Wang, Z. Wu, Z. Sun, L. Li, J. Zhang, W. Hu, M. Hong, J. Luo, Inch-size single crystal of a lead-free organic-inorganic hybrid perovskite for high-performance photodetector, Adv. Funct. Mater. 28 (2018) 1705467.

[51] S. Han, J. Zhang, Z. Sun, C. Ji, W. Zhang, Y. Wang, K. Tao, B. Teng, J. Luo, Lead-free hybrid material with an exceptional dielectric phase transition induced by a chair-to-boat conformation change of the organic cation, Inorg. Chem. 56 (2017) 13078–13085.